Journal of Applied Physics

Revealing carbon mediated luminescence centers with enhanced lifetime in porous alumina

Cite as: J. Appl. Phys. **126**, 164904 (2019); https://doi.org/10.1063/1.5116274
Submitted: 24 June 2019 . Accepted: 13 October 2019 . Published Online: 29 October 2019

S. Bhowmick, S. Pal, A. Singh, M. Gupta, D. M. Phase, A. K. Singh, and A. Kanjilal

View Online Export Citation CrossMark

ARTICLES YOU MAY BE INTERESTED IN

Effective transport properties of conformal Voronoi-bounded columns via recurrent boundary element expansions
Journal of Applied Physics **126**, 164307 (2019); https://doi.org/10.1063/1.5125166

Micromagnetic analysis and optimization of spin-orbit torque switching processes in synthetic antiferromagnets
Journal of Applied Physics **126**, 163905 (2019); https://doi.org/10.1063/1.5121167

Influence of electronic structure parameters on the electrical transport and magnetic properties of $Y_{2-x}Bi_xIr_2O_7$ pyrochlore iridates
Journal of Applied Physics **126**, 165112 (2019); https://doi.org/10.1063/1.5125254

Lock-in Amplifiers
... and more, from DC to 600 MHz
Watch

© 2019 Author(s).

Journal of Applied Physics | ARTICLE | scitation.org/journal/jap

Revealing carbon mediated luminescence centers with enhanced lifetime in porous alumina

Cite as: J. Appl. Phys. **126**, 164904 (2019); doi: 10.1063/1.5116274
Submitted: 24 June 2019 · Accepted: 13 October 2019 ·
Published Online: 29 October 2019

View Online Export Citation CrossMark

S. Bhowmick,[1] S. Pal,[1] A. Singh,[2] M. Gupta,[3] D. M. Phase,[3] A. K. Singh,[2] and A. Kanjilal[1,a)]

AFFILIATIONS

[1]Department of Physics, School of Natural Sciences, Shiv Nadar University, NH-91, Tehsil Dadri, Gautam Buddha Nagar, Uttar Pradesh 201314, India
[2]Materials Research Centre, Indian Institute of Science, Bangalore 560012, India
[3]UGC-DAE Consortium for Scientific Research, Khandwa Road, Indore, Madhya Pradesh 452001, India

[a)]**Author to whom correspondence should be addressed:** aloke.kanjilal@snu.edu.in

ABSTRACT

Carbon ion implantation mediated blue photoluminescence (PL) and the corresponding bluish white phosphorescence of anodic aluminum oxide (AAO) are presented. In particular, the observed 465 nm luminescence is found to be more sensitive to carbon, while its lifetime is raised to its maximum from 6.7 to 10.4 μs at a fluence of 1×10^{16} ions/cm^2. The observed phenomenon seems to be associated with the formation of oxygen vacancy (V_0) via carbon ion enhanced modification of local AlO_6 octahedral symmetry, as revealed from X-ray absorption spectroscopy at O-*K* edge, and also consistent with X-ray photoelectron spectroscopy (XPS). Detailed XPS analysis indicates the preference of carbon at the Al sites, rather than at O for both octahedral and tetrahedral structures, and form C_{Al} cationic impurity, consistent with our density functional theory calculation. Further, carbon ion implantation driven enhanced PL lifetime is shown to be associated with energy transfer between V_0 and the vicinal C_{Al}. This work shows the potential of carbon doped AAO as a future candidate for developing rare earth free nontoxic phosphor.

Published under license by AIP Publishing. https://doi.org/10.1063/1.5116274

INTRODUCTION

Owing to the very reactive nature of aluminum, it is highly probable to oxidize in air and thereby form few nanometer thick oxide layers to prevent it from further oxidation. However, a thicker oxide layer (even up to few micrometers) can be formed on aluminum by electrochemical anodization with desirable engineering properties, such as excellent hardness, abrasion, and corrosion resistance,[1] though it can form either nonporous or porous layers based on the type of electrolytes. Especially, the porous anodized aluminum oxide (AAO) received considerable attention for serving as a good adhesion base for electroplating, semipermanent decorative coloration, and painting.[2] Moreover, AAO with self-ordered hexagonal porous structures have unique optical,[3] electrical,[4] and transport properties,[5] which make them promising for a wide range of applications such as microelectronics,[6] radiation dosimetry,[7] chemical sensor,[8] bio-sensor,[9] drug delivery,[10] etc. Both visible range photoluminescence (PL) and nontoxicity of AAO differentiate it from other materials, and thus, it becomes an extraordinary candidate for label-free biomarker detectors,[11] besides being used as photonic crystals,[12] polarizers,[13] and optical switches.[14] However, porous AAO is not preferred for corrosion protection as the entrapped acid molecules within the pores can itself cause damage to the parent material.[2] The optical properties of amorphous AAO are known to be associated with various defect centers, especially oxygen vacancies (V_O) in different forms such as F center (Vo with two electrons) and F^+ centers (singly ionized oxygen vacancies, Vo) as well as carbon related impurities.[15] In this respect, PL is a promising technique to explain the nature of the defects and their spatial distribution. For instance, Yang *et al.* demonstrate the emission of a broad blue PL band from AAO mostly due to the involvement of F^+ centers,[16] whereas Huang *et al.* reported the importance of both F and F^+ centers in PL.[17] Moreover, Yamamoto *et al.* elucidated the active role of carbon impurity (appears from the oxalic acid under a high electric field) in AAO behind strong PL,[15] but Azevedo *et al.* showed the appearance of weak PL from amorphous AAO when sulfuric acid was employed as an electrolyte.[18] Apart from the reports about strong

Published under license by AIP Publishing.

and tunable luminescence from carbon dots in different environmental states,[19,20] several literatures exist on carbon impurities based luminescent materials like Al_2O_3-SiO_2 porous glasses,[21] carbon doped boron-oxynitride phosphor,[22] yttrium-aluminum-borates,[23] etc. However, the exact role of such carbon in controlling the luminescence mechanism is still not well understood and conclusive. Although the role of carbon impurity in AAO has been examined in some recent theoretical works,[24,25] there is no experimental evidence to identify the exact location of carbon especially to govern the luminescence property. It is, however, known that Al can occupy both tetrahedral (AlO_4) and octahedral (AlO_6) sites in amorphous Al_2O_3 in different proportion where the fraction can be altered by changing electrolytes.[26] A similar phenomenon has also been observed by changing AC to DC voltage during synthesis of AAO layers in sulfuric acid, yielding a (AlO_4)/(AlO_6) ratio of 70:30 and 60:40.[26] However, the porous layers were found to be made of only tetrahedrally coordinated Al or even lower coordination when synthesized in phosphoric acid.[27] Hashimoto *et al.* further showed the formation of porous AAO in sulfuric and oxalic acids containing 50%–60% AlO_5, 30%–40% AlO_4, and 4%–15% AlO_6 polyhedral units.[28] Nevertheless, it has been shown recently that lower coordinated polyhedral units and so V_O can be introduced in the metal oxide due to a sudden loss of ligand O from the octahedral sites.[29] Hence, understanding the type of impurity mediated defects and local structures in governing PL emission is challenging.

In this article, we demonstrate the role of carbon impurity in AAO and the subsequent formation of V_O via local structure modification by carbon ion implantation for achieving controlled PL emission at room temperature (RT). We will show detailed PL and phosphorescence analyses on both as-grown and carbon implanted samples for understanding the mechanism, including PL lifetime. The variation of average lifetime with increasing ion fluence (ions/cm^2) will be discussed in the light of direct participation of V_O and cationic defects C_{Al} and also their cross-talking probability. This will be supported by X-ray photoelectron spectroscopy (XPS) and X-ray absorption spectroscopy (XAS) analyses, especially at the O-*K* and C-*K* edges, and also by density functional theory (DFT) calculation.

EXPERIMENTAL

About 2 μm thick porous AAO layer, with an average pore diameter of ~60 nm [see Fig. 1(a)], was prepared by anodizing 0.1 mm thick aluminum (Al) foil (purity: ~99.99%) using oxalic acid as an electrolyte for 30 min under a constant voltage supply of 30 V with copper as a counter (cathode) electrode, followed by 30 min dipping in 0.5M phosphoric acid.[7] As-grown AAO (Q_0) was implanted at room temperature by 50 keV C^- ions (normal incidence) with fluences of 5×10^{13}, 5×10^{14}, and 1×10^{16} ions/cm^2, where the corresponding samples are named as Q_1, Q_2, and Q_3, respectively, in the following for simplicity. Throughout the experiment, the beam current has been maintained at ~1 μA. The implantation has been carried out in a negative ion implanter at IUAC, New Delhi, India. The Stopping and Range of Ions in Matter (SRIM) calculations have been performed for estimating the depth profile of implanted ions before the experiment,[30] where the distribution of ions inside the Al_2O_3 layers has been shown in Fig. 1(b), showing a maximum penetration depth of 50 keV C^- ions to be ~160 nm.

The pore formation was verified by scanning electron microscopy (SEM) using a TESCAN system (MIRA II LMH). Photoluminescence and phosphorescence measurements were carried out in a Horiba Fluorolog-3 Spectrofluorometer using the 325 nm excitation line of a 450 W Xenon lamp at RT. Time-resolved PL was accomplished in Edinburgh FL920 Fluorescence Life Time Spectrometer. Further, the XPS measurement was carried out in Omicron EA-125 photoelectron spectrometer integrated with a hemispherical analyzer and by using Al-K_α radiation (energy of 1486.6 eV). The calibration of the binding energy (BE) scale was done with respect to the measured kinetic energy of the gold Fermi level. Prior to the XPS measurement, the sample surfaces have been sputtered with 1 keV Ar^+ ions for 10 min to remove the surface contaminants including adsorbed hydrocarbons and water molecules. The local electronic structure was analyzed by XAS at the beamline BL-1 of the Indus-2 synchrotron radiation facility (storage ring energy: 2.5 GeV) at Raja Ramanna Centre for Advanced Technology (RRCAT) Indore, India.

Structural relaxation and electronic structure calculations have been performed using density functional theory (DFT), as

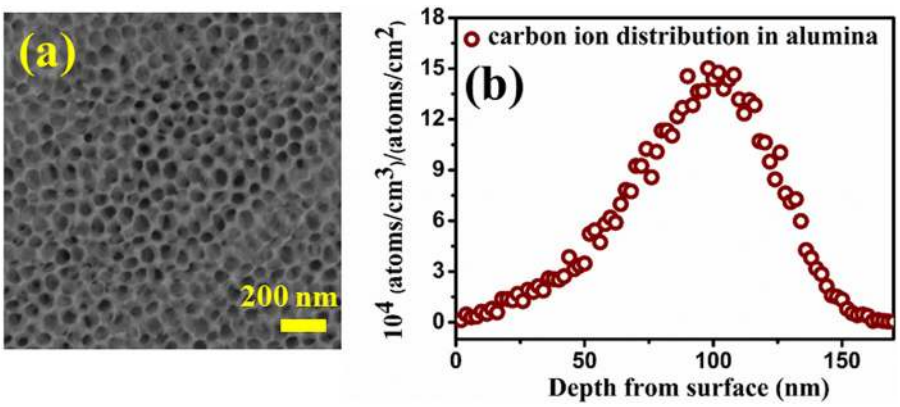

FIG. 1. (a) Top-view SEM image of an as-grown AAO film having an average pore diameter of ~60 nm. (b) The SRIM simulation representing the distribution of 50 keV carbon ion in the alumina layer with the maximum penetration depth to be ~160 nm.

Published under license by AIP Publishing.

implemented in the Vienna *ab initio* simulation package (VASP).[31,32] Perdew-Burke-Ernzerhof (PBE) functional form of the generalized gradient approximation (GGA) for the electronic exchange and correlation is used.[31,33] The kinetic energy cutoff is set to 600 eV for the plane wave expansion of the wave function. All the structures are completely relaxed until the component of the Hellmann-Feynman forces is less than 0.005 eV/Å. We have considered the optimization of cell shape and positions of atoms. Monkhorst-Pack *k*-point mess is used with a very dense grid (9 × 7 × 9) for structural relaxation and the convergence of charge density.

We consider the carbon impurities in octahedral (orthorhombic phase) and tetrahedral (tetragonal phase) sites of Al and O in Al_2O_3. Next, we calculated the defect formation energies of those impurities, which is defined as follows:

$$E^f = E^{Defect}_{total} - E^{bulk}_{total} + \sum n_i \mu_i,$$

where E^{bulk}_{total} is the total relaxed energy of the bulk supercell without defect, E^{Defect}_{total} is the total relaxed energy of the supercell, which contains the defect, n_i is the number of atoms of the ith element that is going to be added to ($n_i > 0$) or removed ($n_i < 0$) from the pristine supercell, and μ_i is the chemical potential of the ith element. A six-unit cell of alumina has been considered for bulk and defect calculations, which contains 30 atoms.

RESULT AND DISCUSSION

Figure 2(a) represents room temperature PL spectra for both as-prepared (Q_0) and ion implanted AAO layers, showing a broad asymmetric PL emission centered at ∼410 nm. All the spectra were deconvoluted independently by Gaussian fitting, where the three fitting components of Q_3 peaking at ∼390, 425, and 465 nm are superimposed for clarity, referred as X, Y, and Z, respectively, in the following. While the origin of X and Y is considered to be associated with V_O with one and two electron(s), called as F^+ and F centers, respectively,[7,34] no considerable attention has yet been given to understand the origin of Z component, except predicting the involvement of carbon impurity from oxalic acid.[15,35] Since no significant change in PL spectra was found here with increasing ion fluence, we further carried out phosphorescence measurement to identify different components by varying the sample window of Q_1 (i.e., detection window length) from 0.5 to 100 ms by keeping the initial delay of 0.1 ms [see Fig. 2(b)]. Note that the phosphorescence measurement is performed here to identify the emission components with relatively long lifetimes.[36] Therefore, with increasing the sample window, the emission component with shorter lifetime will be disappeared by a parallel increase in weightage of the relatively long lifetime components. A gradual shift in peak maximum toward higher wavelength side was found with increasing sample window before reaching the saturation at 70 ms. The deconvolution of the recorded phosphorescence spectra suggests a gradual augmentation of Z (i.e., this component has a longest lifetime) by a parallel suppression of the X and Y peak weightages. Since the Z component is

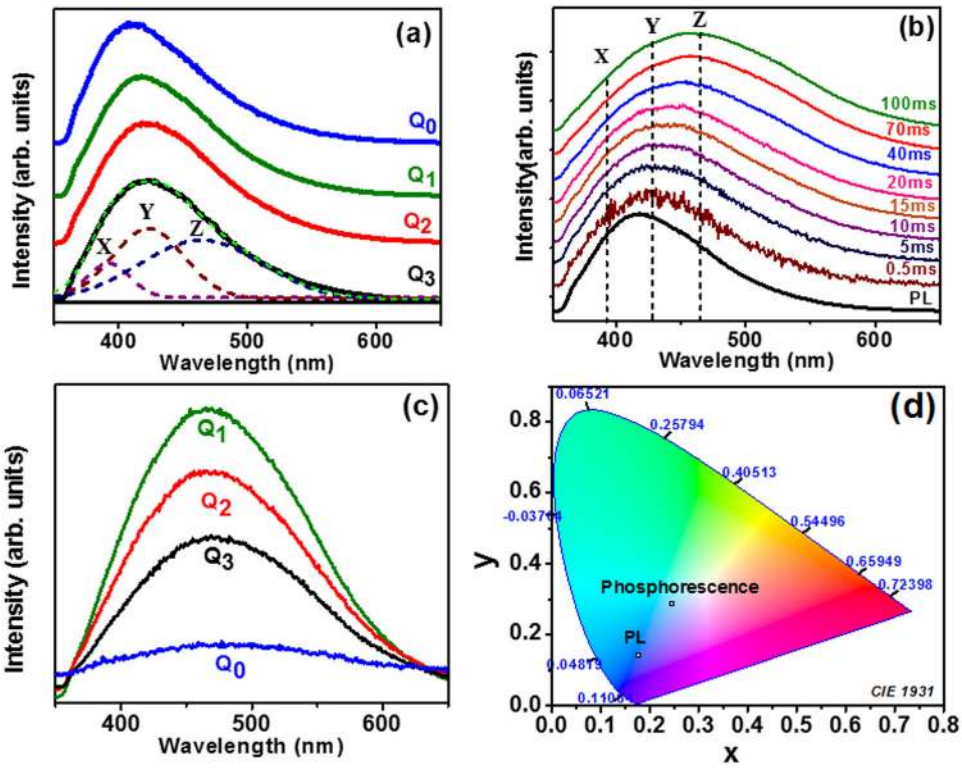

FIG. 2. (a) The PL spectra recorded at RT for both pristine (Q_0) and implanted (Q_1, Q_2, and Q_3) samples. The PL spectra of Q_3 deconvoluted by three Gaussian peaks X, Y, and Z. (b) Recorded phosphorescence spectra of Q_1 by varying the sample window from 0.5 to 100 ms. (c) Phosphorescence from Q_0, Q_1, Q_2, and Q_3, and (d) the chromaticity diagram representing the emission color of both PL and phosphorescence of Q_1.

Published under license by AIP Publishing.

prominent in 70 ms window, the respective spectra for all four samples are plotted in Fig. 2(c) for comparison. A broad emission band with a peak maximum at ∼ 465 nm [resembled with the Z peak in Fig. 2(a)] has been detected to be nonmonotonic in nature with increasing carbon concentration [Fig. 2(c)]. The highest Z peak intensity was found in Q_1, followed by the suppression of intensity with increasing ion fluence. However, the phosphorescence intensity of Q_3 is more than that of Q_0. The origin and the enhancement of Z peak intensity indicate that the associated defect centers are related to the implanted carbon. However, the decrease in peak intensity with increasing carbon ion fluence could be due to the formation of implantation induced nonradiative centers. Further, the chromaticity diagram [Fig. 2(d)] identifies the phosphorescence spectra of the Q_1 sample as bluish white emission in contrast to its deep blue PL emission.

The PL decay curves, recorded at 465 nm, for both pristine and implanted samples are exhibited in Fig. 3, showing a distinct change in shape for Q_3. The changes in other two implanted samples (Q_1 and Q_2) are not that much significant. All decay curves were fitted with multiexponential decay function $I = I_0 + \sum_{i=1}^{n} \beta_i e^{\frac{-t}{\tau_i}}$, where τ is the decay time and β_i represents the exponential fitting amplitudes. The extracted fitting parameters are summarized in Table I, while a typical fitting profile of Q_3 is displayed in the inset of Fig. 3. As can be seen from Table I, each curve was best fitted by three exponential components. The average decay time (τ_{avg}) has also been calculated by $\tau_{avg} = \frac{\sum_{i=1}^{n} \alpha_i \tau_i^2}{\sum_{i=1}^{n} \alpha_i \tau_i}$ for getting an impression of the overall effect of carbon ions on the 465 nm PL emission, where α denotes the relative contribution, determined by $\alpha_i = \frac{\beta_i}{\sum_{i=1}^{n} \beta_i}$ [37] The τ_{avg} of Q_0 is calculated to be ∼6.7 μs, while it reaches to ∼10.4 μs for Q_3. The reason behind the enhancement of τ_{avg} will be discussed in the following.

For understanding the observed PL properties, change in the chemical environment in AAO in the presence of carbon was further investigated by XPS at the O 1*s* and C 1*s* edges. High resolution XPS spectra at the C 1*s* edge for Q_0, Q_1, and Q_3 are exhibited in Fig. 4(a), showing two components [i.e., uncharged carbon (C_{ch}) and charged carbon (C_{uc})], where C_{ch} component is significantly shifted toward the high BE side by ∼5.5 eV due to

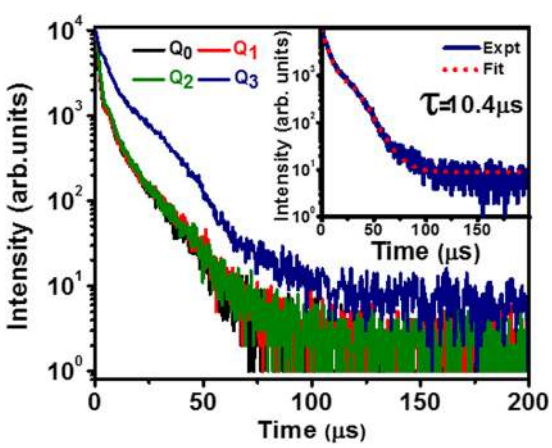

FIG. 3. PL decay curves of Q_0, Q_1, Q_2, and Q_3, where fitted data for Q_3 are shown in the inset.

TABLE I. Fitted data of the PL decay curves of AAO layers before and after carbon ion implantation, where τ and α represent the lifetime and relative contribution of the fitting components, respectively. The average lifetime is τ_{avg}.

Sample	α_1	$\tau_1(\mu s)$	α_2	$\tau_2(\mu s)$	α_3	τ_3 (μs)	τ_{avg} (μs)
Q_0	0.77	1.35	0.16	7.00	0.07	12.71	6.74
Q_1	0.76	1.47	0.17	6.59	0.07	13.43	6.81
Q_2	0.77	1.85	0.16	7.25	0.06	13.41	6.44
Q_3	0.36	5.51	0.19	12.91	0.45	11.03	10.36

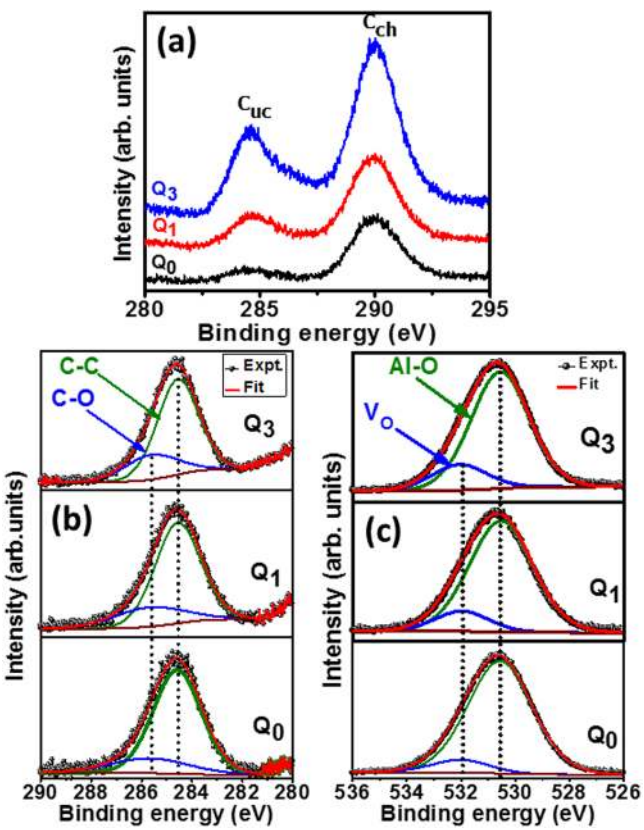

FIG. 4. (a) High resolution C 1*s* core level spectra of Q_0 and carbon implanted (Q_1 and Q_3) samples. (b) Deconvoluted C 1*s* (C_{ch} shifted to characteristic energy) peak for Q_0 (bottom panel), Q_1 (middle panel), and Q_3 (top panel). The experimental data and fitted curves are shown by black circles and thick red lines, respectively. The background subtraction curves are also shown in brown, while the deconvoluted components for C—C and C—O are highlighted by olive green and blue color, respectively. Corresponding deconvoluted O 1*s* peak (after shifting as like in the case of C 1*s*) shown in (c) for Q_0 (bottom panel), Q_1 (middle panel), and Q_3 (top panel).

Published under license by AIP Publishing.

surface charging, while the intensity of the characteristic peak at ~284.5 eV (C_{uc}) from the conducting zone is found to be enhanced gradually with increasing ion fluence. This nonuniform charging in C 1*s* spectra appears due to the presence of two types of carbon atoms: one participates in the formation of the conducting region (C_{uc}) and the other creates bonds in a highly insulating alumina matrix (C_{ch}). This is known as "differential charging" effect, which is beneficial for understanding the chemical states of carbon.[7,38] In fact, when a heterogeneous matrix having at least two regions of different electrical properties is exposed to X-rays, a differential charging effect can occur. This results in developing a positive potential in the less conductive region of the heterogeneous matrix, also known as charging effect. Due to this, the kinetic energy of emitted photoelectrons from an insulating surface decreases and, therefore, shifts the nonconductive component to the higher binding energy region.[39] For detailed understanding, the C_{ch} peak was, therefore, shifted to 284.5 eV before deconvolution in CASA-XPS software using Voigt function (70% Gaussian + 30% Lorentzian) by two components [Fig. 4(b)], representing the existence of C—C (284.5 eV) and C—O (285.6 eV) bonds.[40,41] Note that the Doniach-Sunjic function has often been used to fit the aromatic C 1*s* region from sp^2 carbon, due to the observed asymmetry arising from the interaction of the positive inner core hole with valance electrons.[42,43,44] However, the contributions from the sp^3 C 1*s* signal and other functional groups can be fitted using the standard symmetric fitting protocol with a combination of Lorentzian/Gaussian shape, i.e., Voigt function. Since we are working on the AAO layer doped with C ions, therefore, the contribution of the sp^3 C 1*s* signal would be preferable, especially for the C_{ch} component.[42,43] An estimate about relative percentages of C—C and C—O in samples under investigation is summarized in supplementary material Table S1, documenting a systematic increase of the later component with increasing ion fluence. The key finding is that no C—Al bond formation has been identified in the presently investigating samples. Preferential bonding has been discussed in the following with the help of the DFT calculation. Similarly, O 1*s* spectra were also deconvoluted with two peaks located at ~531.9 and 530.6 eV in the BE scale [see Fig. 4(c)], where the later peak is known to be associated with the oxygen in Al—O bonds[41,45] and the former one is most probably associated with V_O.[46] The fitting results are summarized in supplementary material Table S1, which reflects a systematic rise in the 531.9/530.6 eV peak intensity ratio with increasing fluence.

Moreover, the samples were characterized by XAS, where the typical spectra at the O-*K* edge are displayed in Fig. 5(a). We should note here that in the case of octahedral (tetrahedral) rich complex materials, metal e_g (t_2) makes a strong overlap with the neighboring orbitals of O 2*p*.[47] However, both octahedral and tetrahedral coordination sites exist in different ratios in amorphous Al_2O_3. As discerned, the recorded spectra can be divided into two regimes: (i) 530–545 eV having two main features a_1 and a_2, which are most likely associated with the transitions to the unoccupied mixed states of O 2*p* and crystal-field splitted Al-t_{2g} (e) and Al-e_g (t_2) of Al 3*d*, and (ii) 545–570 eV, marked by a_3, due to the mixing of O 2*p* with Al 4*s* and Al 4*p* states.[47] Interestingly, the a_1 and a_2 peak intensity ratio was found to be altered in the case of Q_3, which resembles well with amorphous Al_2O_3, as reported

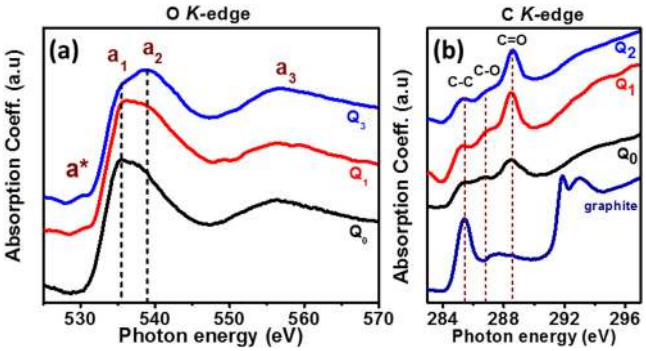

FIG. 5. XAS spectra of (a) O-*K* edge and (b) C-*K* edge for Q_0, Q_1, and Q_3 along with the one for graphite as reference.

previously by Wang *et al.*[48,49] The decrease in the a_1 and a_2 peak intensity ratio in Q_3 further indicates the formation of both penta (AlO_5) and tetra (AlO_4) coordinated Al by deforming the existing AlO_6 octahedra via removal of ligand O (O^{2-}) from the regular position and in turn supports the formation of V_O.[50] The upsurge of V_O with fluence [as stated above in Fig. 4(c)] is also consistent with the rising trend of the pre-edge (marked by a^*) intensity.[51]

The XAS at the C-*K* edge was also examined to understand the average oxidation state and local atomic coordination as a function of ion fluence. The recorded spectra in Fig. 5(b) can be separated into two different regimes: (i) σ^* (>290 eV) and (ii) π^* (<290 eV) states. While the former one comprises C 2*s*, $2p_x$, and $2p_y$ orbitals, the latter one made up of C $2p_z$ orbital is very sensitive to the nature of the functional groups attached to carbon.[52,53] Comparing the XAS spectra of Q_0, Q_1, and Q_3 with (reference) graphite, the peak at ~285.4 eV can be assigned to C—C bonds (transition from 1*s* to π^* in sp^2-bonded carbon), whereas the ones at ~286.5 and ~288.6 eV peaks are associated with π^* components of C—O and C═O, respectively.[54,55]

To understand the local (octahedral or tetrahedral) structure in alumina and preferred site of carbon, we did the DFT calculation using the Vienna *ab initio* simulation package (VASP).[31,32] In the orthorhombic phase [Fig. 6(a)], all the Al atoms are located at octahedral sites. All the Al atoms are surrounded by six oxygen atoms, and the nearest neighbor distance for three of them is 1.98 Å, and for the other three, it is 1.87 Å. The optimized structures of C_{Al} and C_O in the orthorhombic phase of Al_2O_3 are shown in Figs. 6(b) and 6(c), respectively. Moreover, in the tetragonal phase [Fig. 6(d)], all the Al atoms are located at tetrahedral sites. The nearest neighbor distance for two of them is 1.98 Å, and for the other two, it is 1.82 Å. Here, Figs. 6(e) and 6(f) represent the optimized structures of C_{Al} and C_O in the tetragonal phase of Al_2O_3, respectively. The formation energies of C_{Al} (substitution of Al by C) are estimated to be 5.40 and 6.88 eV in tetrahedral and octahedral sites, respectively, and the substitution of O by C atom (i.e., C_O) leads to 10.29 and 10.39 eV for the orthorhombic and tetragonal phases of Al_2O_3, respectively. Therefore, it is clear that carbon prefers the Al site than that of O in any structure, in good agreement with our XPS results in Fig. 4. As the XAS indicates the formation of lower

Published under license by AIP Publishing.

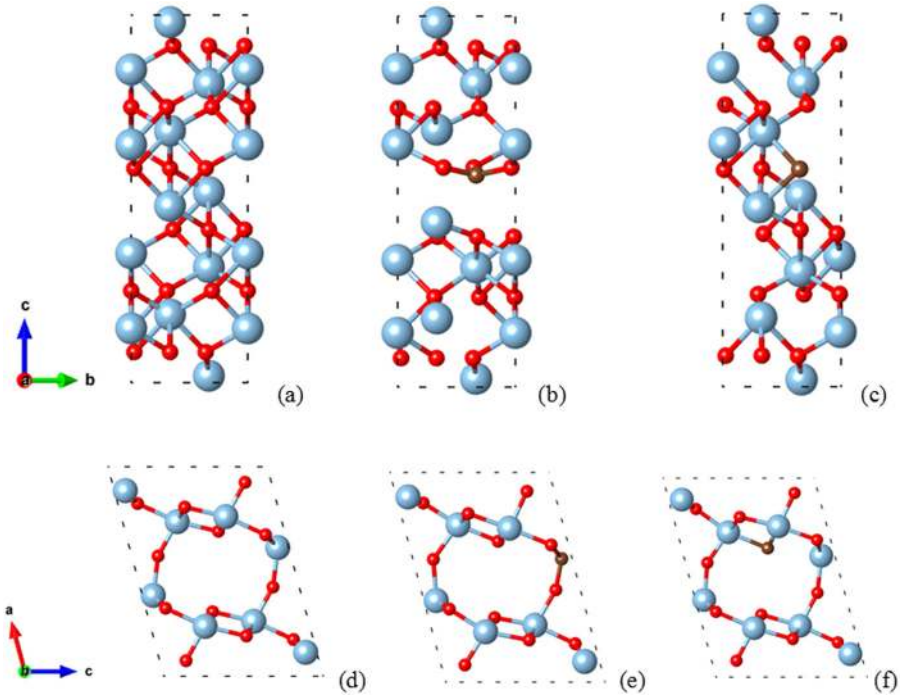

FIG. 6. Optimized orthorhombic structures of Al_2O_3 (a), where the corresponding C_{Al} and C_O are shown in (b) and (c), respectively. Similarly, the optimized tetragonal structure (d) with C_{Al} and C_O are shown in (e) and (f), respectively. Here, Al, O, and C are represented by blue, red, and brown colored solid spheres, respectively.

coordinated polyhedral units with increasing ion fluence, it is, therefore, expected to have more chances of substitution of Al by carbon in tetrahedral sites.

Given the XPS and XAS results, the reason behind the 465 nm PL with longer lifetime than that of F center related 410 nm emission can be understood on the ground of evolution of C_{Al} and V_O in the AAO matrix and the corresponding energy transfer probability with increasing carbon ion fluence. In the case of inorganic insulating phosphors, the delayed fluorescence (phosphorescence) property arises not only for having both intrinsic and extrinsic point defects, but also for their spatial distribution.[56] When dopants act like luminescent centers (LCs), the defect distribution around such LCs can have strong influence on the emission energy, its intensity, and lifetime. But, such distribution of the cationic dopants around anionic vacancies is not random.[56] In our case, XPS result indicates that a fraction of carbon acts as cationic impurities (C_{Al}) as they prefer to sit at Al sites and thereby make bonds with the nearby oxygen atoms. That could be the possible reason behind the enhancement of C—O bonds with increasing ion fluence. The other fraction of carbon, however, does not prefer to go to O site (C_O), while makes bonds to other carbon atoms and causes the observed differential charging. In this context, the ion implantation technique might play a crucial role as this cannot only introduce dopants, but also create intrinsic defects like V_O before terminating into the AAO matrix by losing energy via collision in cascade. This is also consistent with the XAS results at the O-*K* edge, showing ion fluence driven introduction of structural disorder leading to the formation of V_O and also with the O 1*s* XPS analysis. It appears from our study that the concentration and interaction of both C_{Al} and V_O are maximum in Q_3.

This is also reflected in the average lifetime (τ_{avg}) including the individual component and their relative weight percentages (see Table I), where the reason behind the observed variation for the 465 nm PL emission can be discussed in the framework of three possible optical transition processes. We believe that τ_1 would be associated with V_O itself as this has also been detected in Q_0. But, the second and third components, τ_2 and τ_3, are most probably governed by the involvement of C_{Al} and V_O. This is also in agreement with the relative weightage of the respective components. One can also see that V_O dominates in Q_0 (as reflected from α_1) and reduces significantly in Q_3 due to parallel rise in C_{Al}-V_O emission channels by doping carbon impurity. Since very few V_O comes close to C_{Al} centers in Q_1 and Q_2, the active participation of the C_{Al}-V_O emission channels cannot dominate. A drastic variation can only happen at the highest ion fluence (Q_3), as it is expected that the majority of V_O are situated in close vicinity of C_{Al} and thereby accelerating the energy transfer process. In fact, comparing the present PL results with the recorded XAS, it appears that most of the newly created V_O under ion bombardment are participating in forming the C_{Al}-V_O emission channels, instead of forming vacancy clusters. However, we cannot discard the possibility of radiative recombination of electrons and holes within the isolated V_O, which are staying apart from the C_{Al} sites. Note that the individual lifetime (τ_3) of C_{Al}-V_O is comparatively low in Q_3. As the C_{Al} and V_O are more in number, the chances of pair formation are more, and for the same reason, the average distance should be less. This, as a result, lowers the lifetime of the individual defect state.[56] At the same time, the increase of τ_1 value could be due to the change in the local structure around V_O as supported by the pre-edge feature in XAS spectra (Fig. 5).

Published under license by AIP Publishing.

CONCLUSIONS

In summary, we demonstrate the emission of blue PL and the corresponding bluish white phosphorescence of AAO by controlled carbon ion implantation up to a fluence of 1×10^{16} ions/cm^2. Detailed C 1*s* XPS analysis showed the formation of cationic impurity (C_{Al}) in carbon implanted AAO, in agreement with our theoretical results, while O 1*s* analysis reveals the monotonic rise of V_O with increasing ion fluence. Further, the XAS measurement at the O-*K* edge revealed the modification of the local structure, especially the appearance of pre-edge, which was elucidated on the framework of the formation of V_O with increasing ion fluence. A direct correlation between C_{Al} and V_O was shown to be responsible for 465 nm PL emission, while the lifetime measurement confirmed the increase in average lifetime from ~6.7 to ~10.4 μs up to a fluence of 1×10^{16} ions/cm^2. Finally, the observed phosphorescence has been discussed in the light of energy transfer between V_O and C_{Al}. The present observations altogether indicate that carbon implanted AAO could be the benchmark for future development of AAO based nontoxic phosphor.

SUPPLEMENTARY MATERIAL

See the supplementary material for the fitted values of the XPS spectra of the O 1*s* and C 1*s* lines before and after carbon doping in porous alumina (Table S1).

ACKNOWLEDGMENTS

The authors would like to acknowledge the financial support received from Shiv Nadar University and also from DAE-BRNS, India, under Project No. 34/14/24/2016-BRNS/34365. The help received from the scientists at IUAC is acknowledged, especially Mrs. K. D. Devi for ion implantation, Dr. S. A. Khan for helping in SEM measurement, and Dr. D. Kanjilal for valuable suggestions. The help received from Dr. Neetu Singh at AIRF, JNU, New Delhi, India, during time-resolved PL measurement is acknowledged. We are also thankful to Dr. C. P. Saini, IUAC, India, and Mr. D. Das and Mr. D. Kundu, SNU, India, for valuable discussion.

REFERENCES

[1] W. Lee and S.-J. Park, Chem. Rev. **114**, 7487 (2014).
[2] R. Senbahavalli, S. Mohanapriya, and V. Raj, Mater. Discovery **3**, 29 (2016).
[3] C. S. Law, S. Y. Lim, A. D. Abell, L. F. Marsal, and A. Santos, Nanoscale **10**, 14139 (2018).
[4] S. Basu, S. Chatterjee, M. Saha, S. Bandyopadhay, K. K. Mistry, and K. Sengupta, Sens. Actuators B **79**, 182 (2001).
[5] F. Kargar, S. Ramirez, B. Debnath, H. Malekpour, R. K. Lake, and A. A. Balandin, Appl. Phys. Lett. **107**, 171904 (2015).
[6] D. N. Davydov, P. A. Sattari, D. AlMawlawi, A. Osika, T. L. Haslett, and M. Moskovits, J. Appl. Phys. **86**, 3983 (1999).
[7] S. Bhowmick, S. Pal, D. Das, V. K. Singh, S. A. Khan, R. Hübner, S. R. Barman, D. Kanjilal, and A. Kanjilal, J. Appl. Phys. **124**, 134902 (2018).
[8] T. Akiyama, Y. Ishikawa, and K. Hara, Sens. Actuators B **181**, 348 (2013).
[9] L. Pol, C. Eckstein, L. K. Acosta, E. Xifré-Pérez, J. Ferré-Borrull, and L. F. Marsal, Nanomaterials **9**, 478 (2019).
[10] E. Gultepe, D. Nagesha, S. Sridhar, and M. Amiji, Adv. Drug Deliv. Rev. **62**, 305 (2010).
[11] X. Liu, M. Wei, Y. Liu, B. Lv, W. Wei, Y. Zhang, and S. Liu, Anal. Chem. **88**, 8107 (2016).
[12] J. Choi, Y. Luo, R. B. Wehrspohn, R. Hillebrand, J. Schilling, and U. Gösele, J. Appl. Phys. **94**, 4757 (2003).
[13] M. Saito, M. Kirihara, T. Taniguchi, and M. Miyagi, Appl. Phys. Lett. **55**, 607 (1989).
[14] C.-H. Huang, H.-Y. Lin, B.-C. Lau, C.-Y. Liu, H.-C. Chui, and Y. Tzeng, Opt. Express **18**, 27891 (2010).
[15] Y. Yamamoto, N. Baba, and S. Tajima, Nature **289**, 572 (1981).
[16] M. D. Yang, K. W. Chen, J. L. Shen, J. C. Wang, and C. Hsu, Nanotechnology **18**, 405707 (2007).
[17] G. S. Huang, X. L. Wu, Y. F. Mei, X. F. Shao, and G. G. Siu, J. Appl. Phys. **93**, 582 (2003).
[18] W. M. De Azevedo, G. B. De Oliveira, E. F. da Silva, Jr., H. J. Khoury, and E. F. Oliveira de Jesus, Radiat. Prot. Dosim. **119**, 201 (2006).
[19] C.-L. Shen, J.-H. Zang, Q. Lou, L.-X. Su, Z. Li, Z.-Y. Liu, L. Dong, and C.-X. Shan, Carbon **136**, 359 (2018).
[20] Z. Su, H. Ye, Z. Xiong, Q. Lou, Z. Zhang, F. Tang, J. Tang, J. Dai, C. Shan, and S. Xu, Carbon **126**, 58 (2018).
[21] T. Hayakawa, A. Hiramitsu, and M. Nogami, Appl. Phys. Lett. **82**, 2975 (2003).
[22] L. Wang, J. Zhang, B. Qu, Q. Wu, R. Zhou, D. Li, B. Zhang, M. Ren, and X. C. Zeng, Carbon **122**, 176 (2017).
[23] A. D. Sontakke, A. Ferrier, P. Burner, V. F. Guimarães, M. Salaün, V. Maurel, I. Gautier-Luneau, A. Ibanez, and B. Viana, J. Phys. Chem. Lett. **8**, 4735 (2017).
[24] H. D. Tailor, J. L. Lyons, M. Choi, A. Janotti, and C. G. Van de Walle, J. Vac. Sci. Technol. A **33**, 01A120 (2015).
[25] J. Zhu, K. P. Muthe, and R. Pandey, J. Phys. Chem. Solids **75**, 379 (2014).
[26] Y. Oka, T. Takahashi, K. Okada, and S. Iwai, J. Non Cryst. Solids **30**, 349 (1979).
[27] G. Gutierrez and B. Johansson, Phys. Rev. B **65**, 104202 (2002).
[28] H. Hashimoto, K. Yazawa, H. Asoh, and S. Ono, J. Phys. Chem. C **121**, 12300 (2017).
[29] S. J. Stewart, M. Fernández-García, C. Belver, B. S. Mun, and F. G. Requejo, J. Phys. Chem. B **110**, 16482 (2006).
[30] J. F. Ziegler, M. D. Ziegler, and J. P. Biersack, Nucl. Instrum. Methods Phys. Res. B **268**, 1818 (2010).
[31] G. Kresse and J. Furthmüller, Phys. Rev. B **54**, 11169 (1996).
[32] M. Fuchs and M. Scheffler, Comp. Phys. Commun. **119**, 67 (1999).
[33] J. P. Perdew, K. Burke, and M. Ernzerhof, Phys. Rev. Lett. **80**, 891 (1998).
[34] W. L. Xu, M. J. Zheng, S. Wu, and W. Z. Shen, Appl. Phys. Lett. **85**, 4364 (2004).
[35] I. Vrublevsky, K. Chernyakova, A. Ispas, A. Bund, N. Gaponik, and A. Dubavik, J. Lumin. **131**, 938 (2011).
[36] B. Straughan and S. Walker, *Spectroscopy* (Springer, 1976), p. 161.
[37] Y.-C. Chen, K. Katsumata, Y.-H. Chiu, K. Okada, N. Matsushita, and Y.-J. Hsu, Appl. Catal. A **490**, 1 (2015).
[38] J. M. Gorham, W. A. Osborn, J. W. Woodcock, K. C. K. Scott, J. M. Heddleston, A. R. H. Walker, and J. W. Gilman, Carbon **96**, 1208 (2016).
[39] M. P. Seah and D. Briggs, *Practical Surface Analysis: Auger and X-ray Photoelectron Spectroscopy* (John Wiley & Sons, 1990).
[40] D. Tang, J. Su, Q. Yang, M. Kong, Z. Zhao, Y. Huang, X. Liao, and Y. Liu, RSC Adv. **5**, 55170 (2015).
[41] K. Shimizu, C. Phanopoulos, R. Loenders, M.-L. Abel, and J. F. Watts, Surf. Interface Anal. **42**, 1432 (2010).
[42] A. Kovtun, D. Jones, S. Dell'Elce, E. Treossi, A. Liscio, and V. Palermo, Carbon **143**, 268 (2019).
[43] H. Estrade-Szwarckopf, Carbon **42**, 1713 (2004).
[44] S. Doniach and M. Sunjic, J. Phys. C Solid State Phys. **3**, 285 (1970).
[45] A. K. Nanda, S. Prasanna, B. Subramanian, S. Jayakumar, and G. M. Rao, J. Appl. Phys. **117**, 125307 (2015).
[46] G. Yang, D. Gao, J. Zhang, J. Zhang, Z. Shi, and D. Xue, J. Phys. Chem. C **115**, 16814 (2011).
[47] E. O. Filatova and A. S. Konashuk, J. Phys. Chem. C **119**, 20755 (2015).

Published under license by AIP Publishing.

[48]C. Århammar, A. Pietzsch, N. Bock, E. Holmström, C. M. Araujo, J. Gråsjö, S. Zhao, S. Green, T. Peery, F. Hennies, S. Amerioun, A. Föhlisch, J. Schlappa, T. Schmitt, V. N. Strocov, G. A. Niklasson, D. C. Wallace, J.-E. Rubensson, B. Johansson, and R. Ahuja, Proc. Natl. Acad. Sci. U.S.A. **108**, 6355 (2011).
[49]Z. Wang, C. Li, L. Liu, and T.-K. Sham, J. Chem. Phys. **138**, 084706 (2013).
[50]C. P. Saini, A. Barman, D. Banerjee, O. Grynko, S. Prucnal, M. Gupta, D. M. Phase, A. K. Sinha, D. Kanjilal, and W. Skorupa, J. Phys. Chem. C **121**, 11448 (2017).
[51]E. O. Filatova, A. S. Konashuk, F. Schaefers, and V. V. Afanas' ev, J. Phys. Chem. C **120**, 8979 (2016).
[52]J. Boese, A. Osanna, C. Jacobsen, and J. Kirz, J. Electron Spectrosc. Relat. Phenom. **85**, 9 (1997).
[53]X. Weng, P. Rez, and H. Ma, Phys. Rev. B **40**, 4175 (1989).
[54]J. G. Zhou, J. Wang, C. L. Sun, J. M. Maley, R. Sammynaiken, T. K. Sham, and W. F. Pong, J. Mat. Chem. **21**, 14622 (2011).
[55]C.-H. Chuang, Y.-F. Wang, Y.-C. Shao, Y.-C. Yeh, D.-Y. Wang, C.-W. Chen, J. W. Chiou, S. C. Ray, W. F. Pong, and L. Zhang, Sci. Rep. **4**, 4525 (2014).
[56]F. Clabau, X. Rocquefelte, T. Le Mercier, P. Deniard, S. Jobic, and M.-H. Whangbo, Chem. Mater. **18**, 3212 (2006).

Published under license by AIP Publishing.